Coherent random lasing in the deep blue from self-assembled organic nanofibers

A. Andreev[a)]
Institute for Semiconductor and Solid State Physics, University Linz, A-4040 Linz, Austria and Institute of Physics, University of Leoben, A-8700 Leoben, Austria

F. Quochi, F. Cordella, A. Mura, and G. Bongiovanni
Dipartimento di Fisica, Università di Cagliari, I-09042 Monserrato (CA), Italy

H. Sitter
Institute for Semiconductor and Solid State Physics, University Linz, A-4040 Linz, Austria

G. Hlawacek and C. Teichert
Institute of Physics, University of Leoben, A-8700 Leoben, Austria

N. S. Sariciftci
Linz Institute for Organic Solar Cells (LIOS), Physical Chemistry, University Linz, Linz, Austria

(Received 29 June 2005; accepted 29 November 2005; published online 6 February 2006)

We report on the morphological and nonlinear optical properties of highly ordered *para*-sexiphenyl nanofibers grown by hot-wall epitaxy on muscovite mica. For suitable substrate temperatures and deposition times, needle-shaped aggregates are obtained. These nanoaggregates, which are formed by regrouping of small islands of the material, can support optical waveguiding and amplification of the deep-blue emission of *para*-sexiphenyl. We show evidence of low-threshold coherent random lasing in ensembles of nanofibers and study the dependence of lasing on the nanofibers' film thickness. We also present spatially resolved lasing measurements on individual nanofiber segments. The achievement of isolated nanofibers with suitable morphology and low optical losses could open the route to unprecedented photonic and optoelectronic devices at the submicrometric scale. © *2006 American Institute of Physics*. [DOI: 10.1063/1.2161803]

I. INTRODUCTION

In recent years, there has been a great deal of research devoted to the fabrication and characterization of thin films of self-assembled molecular nanoaggregates. Deep understanding and control of the self-aggregation processes of organic molecules yielding efficient optical emission, nonlinear activity, and high optical gain would, in fact, enable the realization of nanoscaled photonic[1] and optoelectronic devices.[2] Tailoring of the nanoaggregates' morphology could also be exploited to attain photonic nanoprobes for environmental and chemical sensing.[3] Among the challenges of today's nanotechnologies, including molecular self-assembly techniques,[4] is thus the realization of nanoaggregates having well-controlled morphological, photonic, and electronic properties and their large-scale integration in arrays and circuits with broad application capabilities.

Recent advances in the field of light-emitting organic nanoaggregates include self-assembling of linear[5,6] and ring-shaped[7] nanostructures based on *para*-sexiphenyl (*p*-6P) and other oligomers. Such nanoaggregates possess truly submicrometric cross-sectional dimensions; variation in shape, size, and surface (film) density of the nanoaggregates has also been obtained by varying the growth conditions[5,6,8] and by laser irradiation techniques.[9] Besides waveguiding in the deep blue,[5,10] a number of optical functions have been demonstrated in *p*-6P self-assembled nanoaggregates, i.e., two-photon processes,[7,11] resonance Raman gain,[12] gain narrowing,[13] and laser-like emission,[14] suggesting that *p*-6P nanoaggregates have potential for photonic applications.

We report a detailed study of the deep-blue coherent emission of highly ordered *p*-6P thin films consisting of one-dimensional self-assembled nanofibers under ultrafast photopumping. The nanofibers are grown by hot-wall epitaxy (HWE) on freshly cleaved mica. In contrast to common deposition methods such as flash evaporation[5] or organic molecular-beam deposition,[7,9–11] the HWE technique, which was developed in our laboratory,[15] allows to grow epitaxial layers close to thermodynamic equilibrium, which is most important for van der Waals epitaxy.[6a,8] As a consequence, the large organic molecules can find the most suitable arrangement before being incorporated into the crystal lattice, resulting in highly ordered structures of the deposited organic layers.[6a,8,16,17] We show both ensemble-averaged and spatially resolved optical measurements, which are complemented by detailed atomic force microscopy (AFM) characterization to define the nanomorphology of the *p*-6P films.

II. EXPERIMENT

As substrates we use freshly cleaved (001)-oriented muscovite mica. *p*-6P is purified by threefold sublimation under dynamic vacuum. The base pressure during growth is about 6×10^{-6} mbar and the *p*-6P source temperature is fixed at 240 °C. The substrate temperature is 130 °C. The growth

[a)]Author to whom correspondence should be addressed; FAX: +43 3842 402 4602; electronic mail: andrey.andreev@mu-leoben.at

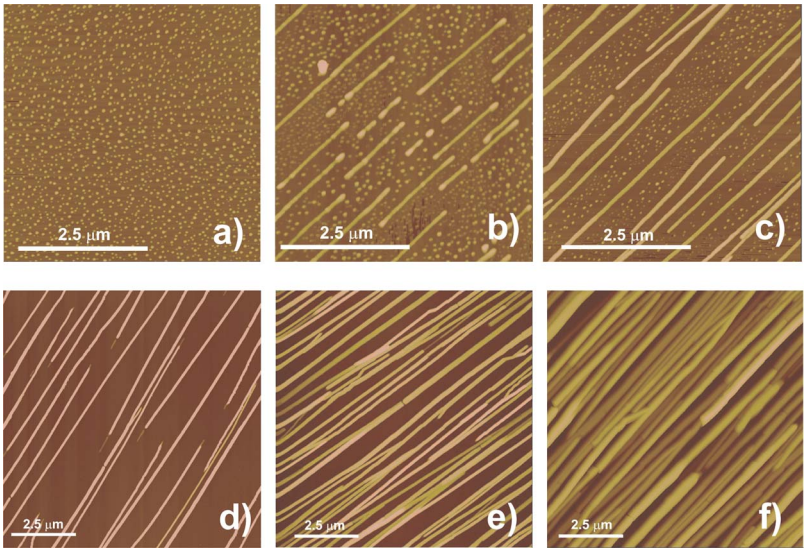

FIG. 1. (Color online) AFM topography images of the *p*-6P films grown within (a) 10 s, (b) 25 s, (c) 90 s, (d) 5 min, (e) 40 min, and (f) 120 min. The growth temperature was 130 °C. The *Z* scale is 0–50 nm in (a)–(c), 0–100 nm in (d), 0–220 nm in (e), and 0–700 nm in (f).

time is varied between 10 s and 120 min. Further growth details can be found in Refs. 6a,8,16. The film morphology is imaged by AFM (Digital Instruments Multimode IIIa and Dimensions 3100) operated in tapping mode in air.

Ultrafast photoexcitation of the *p*-6P samples is performed using the frequency-doubled pulses of a Ti:sapphire regenerative amplifier (150 fs pulses at 760 nm) operating at the repetition frequency of 1 kHz. The polarization of the 380 nm laser beam is set parallel to the long molecular axis of *p*-6P for maximum material absorption. The samples are placed inside a recirculating-loop cold-finger cryostat for optical measurements in the 30–300 K temperature range. The optical emission is collected at different angles by variable numerical aperture optics and wavelength dispersed in an imaging spectrograph with a focal length of 46 cm. A LN_2-cooled charge-coupled device (CCD) is used as the detector.

For ensemble-averaged measurements, the excitation beam is focused to a spot size of about 120 μm. For spatially resolved measurements, the pump spot size is about 180 μm. The emission is collected with a 32× microscope objective and imaged directly onto the input focal plane of the spectrograph. The spectrograph+CCD system allows us (i) to acquire a two-dimensional image of the sample luminescence with a linear resolution of about 2 μm (with the spectrograph set to zeroth-order diffraction) and (ii) to measure emission spectra (with a spectral resolution of about 0.2 nm) as a function of the longitudinal position along nanofibers oriented parallel to the input slit of the spectrograph.

III. RESULTS AND DISCUSSION

It is well known that surface morphology and crystalline quality of *p*-6P films are very crucial for their emitting properties.[5,10,18,19] The HWE technique allows us to control these parameters very well. For example, the surface morphology of *p*-6P films prepared with increasing growth times in the range from 10 s to 120 min are shown in the AFM images of Fig. 1. As depicted in Fig. 1(a) only small uniformly distributed islands can be detected for the sample grown within 10 s. The surface morphology changes drastically if a critical density of islands is reached between 10 and 25 s of growth time: a rearrangement of islands occurs resulting in self-organized nanofibers with micrometer length [Fig. 1(b)]. As shown in Figs. 1(b)–1(f), with increasing time these fibers become progressively longer, quickly reaching a fixed asymptotic width. At least after 5 min of growth nearly no small islands could be found on the surface [Fig. 1(d)], while the fibers become closer to each other.

Figure 2 shows a high-resolution three-dimensional (3D) AFM image of a single *p*-6P nanofiber surrounded by small *p*-6P islands in the most interesting intermediate growth stage, where islands and fibers coexist. The image clearly reveals that the roughly 850-nm-long, 15-nm-high, and 75-nm-wide fiber is not homogeneous and consists of about 15 small blocks with approximately the same size as free standing *p*-6P islands. This result indicates that self-organized fibers on mica are formed by regrouping of mobile individual islands/crystallites originating from earlier growth stages. This thesis is well supported by the observation (using dark-field electron microscopy) of different crystalline *p*-6P domains within long *p*-6P nanofibers.[20]

As the results are clear from Figs. 1(b)–1(f), from the very beginning all fibers are strictly parallel to each other

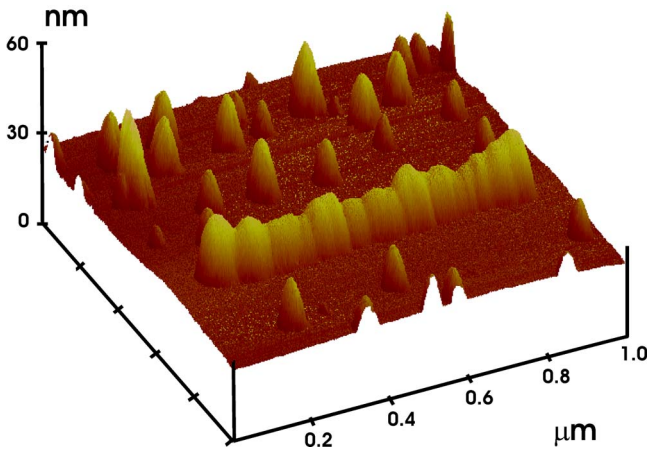

FIG. 2. (Color online) High-resolution three-dimensional AFM image showing individual *p*-6P islands as well as a single nanofiber.

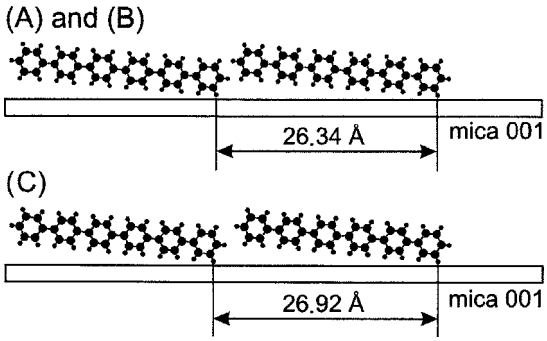

FIG. 3. Side view of *p*-6P molecules relative to the mica (001) substrate as they are oriented within their epitaxial orientations. Top part: Orientations (A) and (B) with the same intermolecular distance of $a=26.34$ Å. Bottom part: Orientation (C) with another distance of $a=26.92$ Å.

having the same preferential orientation relative to the substrate. Detailed AFM investigations show that this orientation as well as *p*-6P island nucleation are not controlled by step edges on the mica surface. Moreover, x-ray diffraction (XRD) and transmission electron diffraction studies reveal three similar crystallographic orientations of *p*-6P on mica (both for fibers and islands): $(11-1)$ *p*-6P$\|(001)$ mica and $[1-2-1]$ *p*-6P$\|[-340]$ mica [orientation (A)]; $(-1-11)$ *p*-6P$\|(001)$ mica and $[-110]$ *p*-6P$\|[-340]$ mica [orientation (B)] and $(11-2)$ *p*-6P$\|(001)$ mica and $[-20-1]$*p*-6P$\|[-310]$ mica [orientation (C)].[16,20] These three orientations of the molecules relative to the substrate are shown in Fig. 3. In all three cases the alignment of *p*-6P molecules relative to the substrate and to each other is approximately the same: their long axes within the fibers are nearly parallel to the substrate and perpendicular to the needle's direction. A high degree of epitaxial alignment is proven by rocking curves with a full width at half maximum (FWHM) as narrow as 0.06°.[21]

In order to obtain detailed geometrical information about the nanofibers, their height and width distributions are measured using AFM. Results are summarized on the histograms in Fig. 4 for the two *p*-6P films grown within 40 and 120 min [see Figs. 1(e) and 1(f). One can see that with increasing growth time from 40 to 120 min the average fiber's height $\langle h\rangle$ increases almost linearly from ≈110 to ≈290 nm, while its width $\langle b\rangle$ increases much slower from ≈210 to ≈350 nm. Moreover, if more material is deposited, both the fiber height and width distributions become broader, clearly indicating a strong increase of fiber size fluctuations (i.e., morphological inhomogeneity of the *p*-6P film surface).

Laser action is investigated using photopumping with ultrashort pulses on samples with increasing film deposition time to study the dependence of lasing on the nanofibers' average size. All measurements are done at room temperature. The emission is found to be rather isotropic due to strong light scattering by the nanostructured surface of the samples. Optical collection is done normally to the sample surface with an *f*-number (f/N) of about 4. The results are substantially independent of both the collection angle and f/N value. The emission features a degree of linear polarization (parallel to the long molecular axis of *p*-6P) of 7 dB or larger across the entire emission spectral window, consistent with the high degree of orientation of the nanofibers and their high crystallinity.

As a first step, experiments are performed in the *ensemble-average* configuration: the exciting laser beam is

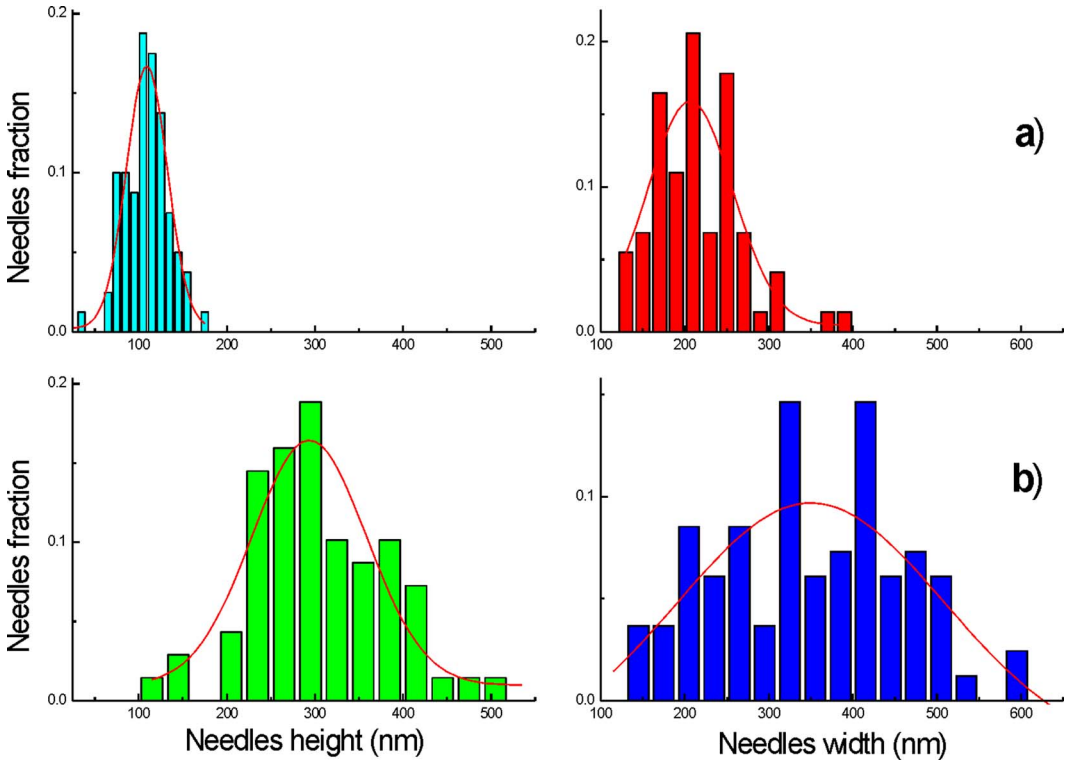

FIG. 4. (Color online) Nanofiber dimensions for the *p*-6P films grown within 40 (a) and 120 min (b). Left: Experimental fiber height distributions (bar graphs) with corresponding gauss distributions (closed lines); right: corresponding width distributions.

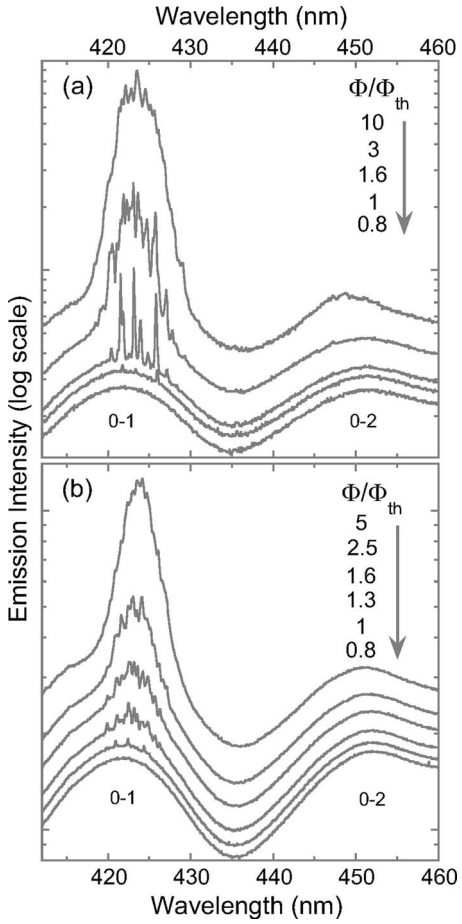

FIG. 5. (a) Room-temperature emission spectra of the *p*-6P nanofibers with $\langle h \rangle \approx 110$ nm (sample *E*) for different values of the pump fluence Φ/Φ_{th} ($\Phi_{th} \approx 1\ \mu J/cm^2$ per pulse). (b) Same as in panel (a) but measured in the sample with $\langle h \rangle \approx 290$ nm (sample *F*, $\Phi_{th} \approx 6\ \mu J/cm^2$).

(i) focused on the sample to a spot whose size ($\sim 120\ \mu m$) is much larger than the cross-sectional dimension of the nanofibers, hence allowing to pump a fairly large number of nanofibers; (ii) the emission from the entire spot is collected and spectrally resolved to get the response of the nanofibers' ensemble.

No evidence for nonlinear emission is seen when the fibers are at early stages of nucleation [Figs. 1(a)–1(c)] since their cross-sectional size is far too small to enable waveguiding of light beyond 400 nm of wavelength.[10] Although nicely shaped fibers are realized with a deposition time of 5 min, neither nonlinear narrowing nor laser action is detected in the sample reported in Fig. 1(d) (sample *D*) for pump fluences as high as 2 mJ/cm^2. Again, lack of laser action is attributed to poor optical waveguiding due to insufficient fiber width. Statistical analysis of the nanofibers' morphology (not shown) yields $\langle h \rangle \approx 100$ nm and $\langle b \rangle \approx 125$ nm, from which we estimate that in sample *D* the fraction of nanofibers potentially supporting waveguiding at 420 nm is only a few percent.

Figure 5(a) shows ensemble-averaged emission spectra of the sample with $\langle h \rangle \approx 110$ nm [sample *E*, shown in Fig. 1(e)] for different values of the excitation fluence at room temperature. For excitation fluences exceeding threshold values (Φ_{th}) which can be as low as 1 $\mu J/cm^2$ (per pulse), discrete peaks emerge from the spontaneous emission spectrum at the 0-1 vibronic peak near 420 nm. Their linewidth is 0.2 nm or smaller. Due to the *p*-6P film inhomogeneity, fairly large variation in Φ_{th} (up to a factor of 10) is found as the excitation spot is moved across the sample surface. The film absorption being $\approx 30\%$, the surface filling factor $\approx 50\%$, and assuming further that the conversion efficiency of the absorbed pump energy into singlet excitons is equal to 100%, a threshold fluence $\Phi_{th} = 1\ \mu J/cm^2$ is estimated to correspond to a density $N_{th} = 1.2 \times 10^{17}\ cm^{-3}$, which is over four orders of magnitude smaller than the *p*-6P molecular crystal density. However, the long-term stability (over a time period of weeks) is verified only for a threshold fluence of the order of $10-30\ \mu J/cm^2$ [$N_{th} \sim (1-3) \times 10^{18}\ cm^{-3}$). Laser-induced damage of the *p*-6P films can occur after intensive utilization of the samples.

The observed phenomenology is attributed to *coherent* random lasing,[22] arising from recurrent scattering within the system of close-packed nanofibers. As a matter of fact, the nanofibers realize a tight interconnect [Figs. 1(e) and 1(f)] that cannot be traced back to an inhomogeneous ensemble of *independent* fibers. Cracks, bends, sudden variation in fiber height or width, and intersection points between adjacent fiber segments can serve as optical scattering centers. Given the large number of such features, the light diffused by a scatterer can come back to the same scatterer after experiencing a sequence of scattering processes in the *p*-6P nanofiber film, hence forming a closed-loop path for light amplification. Lasing starts when the closed-loop amplification overcomes the loss, provided that the total phase variation in the loop is equal to a integer multiple of 2π. Owing to the randomness of the phase shift experienced by the light in each scattering process and of the distance between scattering centers, lasing occurs at random frequencies. Coherent random lasing with very similar features has been reported over the last decade in a variety of material systems.[23–26] As the pump fluence is increased, a growing number of closed-loop random paths existing within the photoexcited spot reaches threshold, resulting in the appearance of additional discrete peaks in the emission spectrum. This is partially responsible for the superlinear dependence of the emission intensity versus pump fluence above threshold.

In addition to coherent random lasing, as the pump intensity is increased, optical gain exceeds the losses in an increasing number of open-loop paths, yielding intensity (or *incoherent*) amplification, namely, amplified spontaneous emission (ASE). ASE, in turn, is responsible for line narrowing and possibly overlaps with coherent random lasing, thereby reinforcing the superlinear growth of the emission intensity.

Very similar results are obtained in the sample with $\langle h \rangle = 290$ nm [sample *F*, shown in Fig. 1(f)], as reported in Fig. 5(b). The larger film inhomogeneity of this sample is responsible for an increased efficiency of light scattering into out-of-plane directions, which do not contribute to the build up of closed-loop paths for coherent random lasing. This might explain why in sample *F* coherent features are less pronounced than in sample *E* and why the threshold pump flu-

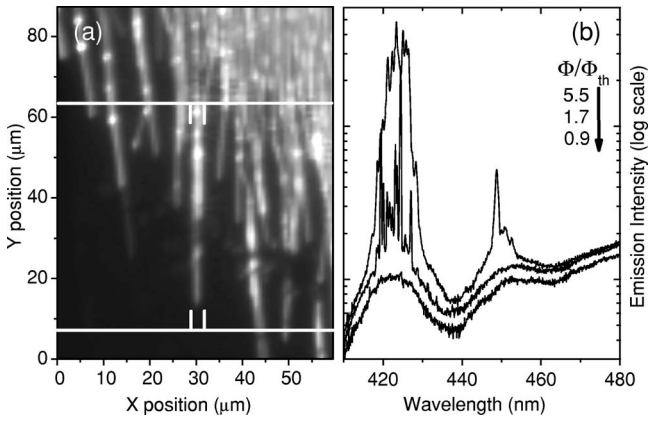

FIG. 6. (a) Gray-scale micrograph of random lasing nanofibers (sample *E*). The excitation fluence is $\approx 60\ \mu J/cm^2$ per pulse. The white markers are delimiters for the area over which the spectra shown in (b) are spatially integrated. (b) Emission spectra measured for different values of the pump fluence Φ/Φ_{th} ($\Phi_{th} \approx 35\ \mu J/cm^2$).

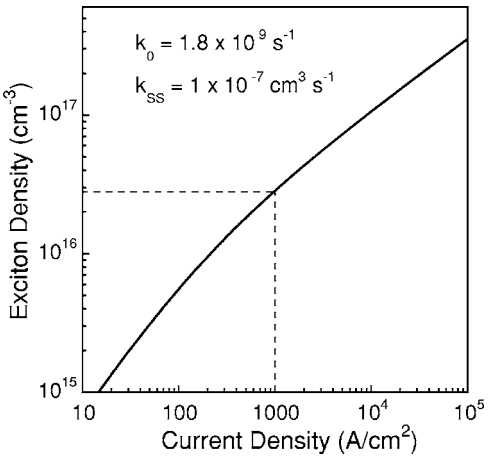

FIG. 7. Exciton density vs estimated dc current density. The current density is estimated assuming a singlet-to-triplet ratio of 0.3 and an average nanofiber height of 110 nm. The vertical and horizontal dashed lines mark the current density $J=1\ kA/cm^2$ and the corresponding singlet density $N=3\times10^{16}\ cm^{-3}$, respectively.

ences are higher ($\sim$10–100 $\mu J/cm^2$). Intermediate material deposition times (of a few tens of minutes) are thus inferred to yield nanofibers with lowest losses.

To get better insight into the random lasing properties, we perform *spatially resolved* lasing measurements. A large pump spot ($\approx$180 μm in diameter) is still used, but the emission is spatially resolved with a linear resolution of 2 μm approximately. Care is taken as to excite a spot at the edge of the area covered with *p*-6P, where the nanofiber density is lower. Results relating to this configuration are reported in Fig. 6.

Figure 6(a) shows an emission micrograph taken on sample *E*. The picture covers an area smaller than the excited spot and is taken above threshold so that it displays both spontaneous and coherent emission. One recognizes the shape of a few nanofibers leaning out of the area covered with *p*-6P. We measure the emission spectrum integrated over the small ($3\times56\ \mu m^2$) area delimited by the white markers, that is, over a well-defined nanofiber segment. Spectra are shown for different pump fluences in Fig. 6(b). The results are similar to those observed in ensemble-averaged measurements: discrete random lasing modes emerge from the spontaneous emission spectrum when the threshold fluence is reached. Lasing is observed also at the 0-2 vibronic peak near 450 nm.

Although the spectroscopically singled-out nanofiber segment is not decoupled from the surrounding nanofibers (as being part of the whole fiber interconnect), the strong similarities between the ensemble-averaged spectra and spatially resolved spectra suggest that coherent random lasing in *p*-6P nanofibers has a *one-dimensional* character. Thin cracks and sudden variation in fiber thickness or width can account for the realization of one-dimensional random optical cavities in isolated nanofibers. A detailed study of random lasing in single nanofibers has been carried out very recently.[27]

Below threshold, the exciton recombination dynamics is dominated by density-dependent effects, which are ascribed to singlet-singlet annihilation. This results from the sublinear growth of the emission intensity versus excitation fluence, as in fact revealed in sample E. The singlet-singlet annihilation coefficient (k_{SS}) is estimated to be as high as $10^{-7}\ cm^3\ s^{-1}$, which further confirms the high degree of crystallinity of the nanofibers. The low-intensity recombination rate (k_0), including both radiative and nonradiative losses, amounts to $\approx 1.8\times10^9\ s^{-1}$. Thus, in our system singlet-singlet annihilation loss is estimated to overcome nonradiative loss at a density $\approx 2\times10^{16}\ cm^{-3}$. The physical parameters (k_0, k_{SS}) of crystalline *p*-6P have been obtained upon averaging over a large number of nanofibers placed in different positions on the sample.[14]

Knowing the exciton recombination constants, we can give an estimate for the electrical current density which has to flow through the nanofibers' film to achieve threshold in continuous-wave (cw) operation. The current density at a given exciton population density is derived by imposing that the total formation rate of singlets be equal to the total recombination rate. The estimate is done for sample *E*, where the lowest threshold densities have been found. The thickness of the recombination region is set equal to the average thickness of the nanofibers ($\langle h\rangle = 110$ nm), and the statistical value of 0.3 is taken for the singlet-to-triplet generation ratio. For the recombination rate, density-dependent losses other than singlet-singlet annihilation (e.g., singlet-polaron annihilation) are neglected. This approximation puts a lower limit to the current density required for lasing. The variation in singlet population density with current density is shown in Fig. 7. It turns out that to operate at a current density $J \sim 1\ kA/cm^2$, which is sustainable in high-mobility organic crystals,[28] lasing should start at a density $N_{th}\sim 3\times10^{16}\ cm^{-3}$. This limit is close to the minimum threshold density reported in our samples, suggesting that an electrically driven nanofiber-based laser might be achievable. In addition to density-dependent losses, voltage breakdown should be taken into account for a more quantitative estimate of the maximum current density that can drive the nanofibers. Operation at current densities $<1\ kA/cm^2$ could indeed be necessary, in which case nanofibers should be realized with even lower optical losses.

IV. CONCLUSIONS

In conclusion, we report a detailed account of the morphological and nonlinear optical properties of *p*-6P self-assembled nanofibers grown by HWE on mica. We show the dependence of both the film morphology and nanofiber coverage on deposition time, and how the regrouping process of *p*-6P islands into linear nanofibers takes place. When the nanofibers are photoexcited by ultrafast laser pulses, low-threshold laser-like emission occurs in the deep-blue (420–450 nm) spectral range. Based on the results of both ensemble-averaged and spatially resolved measurements, the nonlinear emission is attributed to coherent random lasing in a system of close-packed nanofibers. Spatially resolved measurements also suggest that nanofiber lasing is one-dimensional. We claim that one-dimensional lasing on the longitudinal modes of isolated and morphologically uniform nanofibers is necessary for practical application of *p*-6P nanofibers as nanolasers. Regarding the feasibility of electrically excited nanofiber-based lasing, our estimates based on the results of the present study are encouraging, although further investigations are necessary to define the requirements for electrical pumping more quantitatively. In the end, the realization of nanofibers having ultralow optical scattering losses, together with the availability of an effective technology for charge-carrier injection into the nanofibers, could enable the realization of electrically driven nanolasers. The present work is thus expected to stimulate further consideration of *p*-6P nanofibers for both photonic and optoelectronic applications at the submicrometric scale.

ACKNOWLEDGMENTS

The authors acknowledge partial support from the Austrian Foundation for Advancement of Scientific Research (FWF Project Nos. P-15155, P-15627, P-15629, and P-15630-N08) and from the Austria/Italy Scientific & Technological Collaboration Program (Project No. 19/2004). Part of this work was performed within the Christian Doppler Society's dedicated laboratory on Plastic Solar Cells funded by the Austrian Ministry of Economic Affairs and Konarka Austria Ges.m.b.H. The authors would like to thank H. Hoppe for help with the AFM measurements and G. Del Fiacco for technical support.

[1] Y. Huang, G. T. Paloczi, J. K. S. Poon, and A. Yariv, Adv. Mater. (Weinheim, Ger.) **16**, 44 (2004).
[2] J. G. C. Veinot, H. Yan, S. M. Smith, J. Cui, Q. Huang, and T. J. Marks, Nano Lett. **2**, 333 (2002).
[3] C.-Y. Chao and L. J. Guo, Appl. Phys. Lett. **83**, 1527 (2003).
[4] M. de Wild, S. Berner, H. Suzuki, L. Ramoino, A. Baratoff, and T. A. Jung, Chimia **56**, 500 (2002).
[5] H. Yanagi and T. Morikawa, Appl. Phys. Lett. **75**, 187 (1999).
[6] A. Andreev, G. Matt, C. J. Brabec, H. Sitter, D. Badt, H. Seyringer, and N. S. Sariciftci, Adv. Mater. (Weinheim, Ger.) **12**, 629 (2000); F. Balzer and H.-G. Rubahn, Appl. Phys. Lett. **79**, 3860 (2001); M. Schiek, A. Lützen, R. Koch, K. Al-Shamery, F. Balzer, R. Frese, and H.-G. Rubahn, *ibid.* **86**, 153107 (2005).
[7] F. Balzer, J. Beermann, S. I. Bozhevolnyi, A. C. Simonsen, and H.-G. Rubahn, Nano Lett. **3**, 1311 (2003).
[8] A. Andreev, H. Sitter, C. J. Brabec, P. Hinterdorfer, G. Springholz, and N. S. Sariciftci, Synth. Met. **121**, 1379 (2001).
[9] F. Balzer, and H.-G. Rubahn, Nano Lett. **2**, 747 (2002).
[10] F. Balzer, V. G. Bordo, A. C. Simonsen, and H.-G. Rubahn, Phys. Rev. B **67**, 115408 (2003).
[11] F. Balzer, K. Al-Shamery, R. Neuendorf, and H.-G. Rubahn, Chem. Phys. Lett. **368**, 307 (2003).
[12] H. Yanagi and A. Yoshiki, Appl. Phys. Lett. **84**, 4783 (2004).
[13] H. Yanagi, T. Ohara and T. Morikawa, Adv. Mater. (Weinheim, Ger.) **13**, 1452 (2001).
[14] F. Quochi *et al.*, Appl. Phys. Lett. **84**, 4454 (2004).
[15] A. Lopez-Otero, Thin Solid Films **49**, 3 (1978).
[16] H. Plank *et al.*, Phys. Rev. B **64**, 235423 (2001).
[17] D. Stifter and H. Sitter, Appl. Phys. Lett. **66**, 679 (1995).
[18] M. Ariu *et al.*, Chem. Phys. Lett. **313**, 405 (1999).
[19] A. Kadashchuk, A. Andreev, H. Sitter, N. S. Sariciftci, Yu. Skryshevski, Yu. Piryatinski, I. Blonsky, and D. Meissner, Adv. Funct. Mater. **14**, 970 (2004).
[20] H. Plank, R. Resel, H. Sitter, A. Andreev, N. S. Sariciftci, G. Hlawacek, C. Teichert, A. Thierry, B. Lotz, Thin Solid Films **443**, 108 (2003); C. Teichert, G. Hlawacek, A. Yu. Andreev, H. Sitter, and N. S. Sariciftci, Appl. Phys. A: Mater. Sci. Process. **82**, 665 (2005).
[21] A. Andreev *et al.*, Mol. Cryst. Liq. Cryst. Sci. Technol., Sect. A **385**, 61 (2002).
[22] H. Cao, J. Y. Xu, S.-H. Chang, and S. T. Ho, Phys. Rev. E **61**, 1985 (2000).
[23] For a review, see, e.g., H. Cao, Waves Random Media **13**, R1 (2003).
[24] S. V. Frolov, Z. V. Vardeny, K. Yoshino, A. Zakhidov, and R. H. Baughman, Phys. Rev. B **59**, R5284 (1999).
[25] H. Cao, Y. G. Zhao, S. T. Ho, E. W. Seelig, Q. H. Wang, and R. P. H. Chang, Phys. Rev. Lett. **82**, 2278 (1999).
[26] M. Anni, S. Lattante, R. Cingolani, G. Gigli, G. Barbarella, and L. Favaretto, Appl. Phys. Lett. **83**, 2754 (2003).
[27] F. Quochi, F. Cordella, A. Mura, G. Bongiovanni, F. Balzer, and H.-G. Rubahn, J. Phys. Chem. B **109**, 21690 (2005).
[28] M. A. Baldo, R. J. Holmes, and S. R. Forrest, Phys. Rev. B **66**, 035321 (2003).